Mott-insulating phases of the Bose-Hubbard model on quasi-one-dimensional ladder lattices

Lorenzo Carfora,[1,*] Callum W. Duncan,[2,1] Stefan Kuhr,[1] and Peter Kirton[1,†]
[1]Department of Physics and SUPA, University of Strathclyde, Glasgow G4 0NG, United Kingdom
[2]Aegiq Ltd., Arundel Street, Sheffield S1 2NS, United Kingdom

(Received 25 February 2026; accepted 13 July 2026; published 3 August 2026)

We calculate the phase diagram of the Bose-Hubbard model on a half-filled ladder lattice including the effect of finite on-site interactions. This shows that the rung-Mott insulator (RMI) phase persists for finite interaction strength, and we calculate the RMI-superfluid phase boundary in the thermodynamic limit. We show that the phases can still be distinguished using the number and parity variances, which are observables accessible in a quantum-gas microscope. Phases analogous to the RMI were found to exist in other quasi-one-dimensional lattice structures, with the lattice connectivity modifying the phase boundaries. This shows that the presence of these phases is the result of states with one-dimensional structures being mapped onto higher-dimensional systems, driven by the reduction of hopping rates along different directions.

DOI: 10.1103/wml6-1kc2

I. INTRODUCTION

Lattice dimensionality and geometry have a profound impact on the physical properties of strongly correlated quantum systems. In ultracold-atom experiments, control over the geometry of the lattice [1–3] has proved instrumental in the investigation of emergent many-body phenomena such as frustration [4,5], nontrivial band structures [6–9], and dimensional crossovers [10–12]. These studies show that ultracold atoms in optical lattices are an ideal platform to demonstrate how dimensionality and lattice geometry affect complex quantum phenomena.

Among these engineered geometries, the ladder lattice has proved to be a useful platform for investigating low-dimensional quantum systems [13–15]. Its quasi-one-dimensional (quasi-1D) structure enables the observation of a crossover from 1D to 2D physics [16], which is especially evident in its response to a magnetic field. For example, the phase transitions between Meissner and vortex phases were both experimentally [17] and theoretically [18–21] observed in ladder lattices. These flux-driven transitions produce rich phase diagrams due to their interplay with population-filling-driven transitions [22–25]. Flux-driven and filling-driven transitions share analogous underlying mechanisms [26,27]. This is because both are related to the commensurability of the states involved. In particular, even in the absence of a magnetic field, the ladder geometry allows for additional commensurate fillings and associated transitions. While the ground state of 1D lattices is a Mott insulator (MI) only at integer fillings [2,28–32], the ladder supports insulating phases at both integer [18,33] and half-integer fillings [34]. The insulating phase which appears at half-integer fillings, induced by strong coupling between the chains, is known as the rung-Mott insulator (RMI).

The critical behavior of ladder systems has been studied via bosonization and renormalization group techniques [26,27,35]. Most of the previous studies of the RMI focused on the hard-core boson (HCB) limit as a way to uncover the differences between Bose and Fermi statistics. While the mapping of HCBs onto spinless fermions is exact in a 1D chain [36], it breaks down in a ladder once interchain couplings are introduced [34]. This gives rise to significant nonlocal interactions, described by complex Hamiltonian terms [37]. Beyond this, the extension of the RMI phase into the soft-core regime has been investigated by considering three-body local constraints for both attractive and repulsive interactions [38,39]. Cluster mean-field and Gross-Pitaevskii approaches have likewise been applied to ladders in the presence of synthetic gauge fields in both the strong and weak magnetic flux limits [19,40]. Although these approximations give a comprehensive picture of the system behavior, they may not reliably capture the nuances of the RMI in more experimentally accessible regimes.

In this work we investigate the transition between the superfluid (SF) and RMI phases at half filling and in the presence of finite on-site interactions. We characterize the system using microscopic observables that are accessible experimentally. We extend the discussion of the RMI phase to analogous insulating phases on different quasi-1D lattices, underlining the connection between filling fraction and dimensionality by relating it to less trivial geometries, such as staggered two-dimensional [41] and triangular [42] lattices. We also provide guidance for future experiments by considering quantities which are directly measurable in quantum-gas microscope experiments with site-resolved *in situ* imaging of atoms [43–48]. In these setups, optical digital mirror devices allow for the design and microscopic control of the lattice geometry [49–51],

*Contact author: lorenzo.carfora.2018@uni.strath.ac.uk
†Contact author: peter.kirton@strath.ac.uk

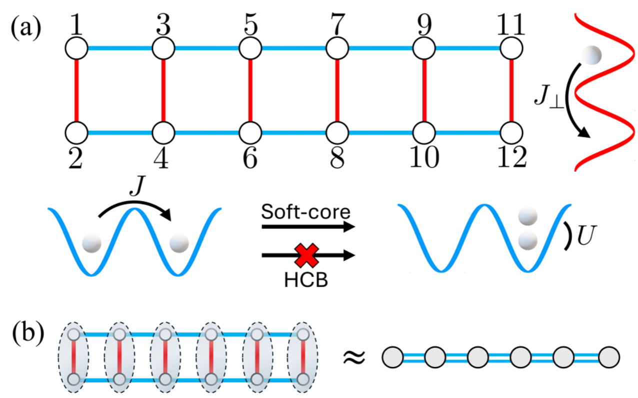

FIG. 1. (a) Geometry of the two-leg ladder. Hopping along each chain occurs at rate J (blue links), while the interchain hopping across the rungs occurs at rate $J_\perp$ (red links). In the HCB limit $U \to \infty$, doubly occupied sites are prohibited. (b) In the RMI phase each boson is delocalized across the two sites of a rung but localized along the chains, leading to insulating behavior. This configuration is analogous to the MI phase of a fully filled single chain with effective hopping amplitude $2J$.

dimensionality, and filling [32,52] via engineered light potentials. Two-leg ladder systems have also been realized using optical superlattices [6,25,53].

The structure of this paper is as follows. We begin in Sec. II by introducing the model and lattice geometry as well as describing the relevant properties of the SF and RMI phases. We then discuss the transition between these phases in Sec. II A, including the extrapolation of the critical phase boundary in the thermodynamic limit. Section II B describes how the different phases can be accessed experimentally, with a particular focus on how the population and parity variances can be used to characterize the system. In Sec. III we examine a wider set of ladderlike lattices, showing how the RMI phase generalizes for different quasi-1D geometries. Section IV presents our conclusions and outlines potential directions for future work.

II. BOSE-HUBBARD MODEL ON A LADDER

We begin by introducing the model describing the behavior of bosons on a ladder lattice. The system is governed by the Bose-Hubbard (BH) [2,29–31] Hamiltonian

$$\hat{H} = \frac{U}{2}\sum_{i}^{M} \hat{n}_i(\hat{n}_i - 1) - \sum_{i,j}^{M} J_{ij}(\hat{a}_i^\dagger \hat{a}_j + \hat{a}_j^\dagger \hat{a}_i), \tag{1}$$

where U is the on-site interaction parameter and J_{ij} is the hopping rate from site i to site j, defined by the lattice geometry through the hopping matrix $\mathbf{J}$. The sum in the second term runs over all pairs of sites which are connected by the lattice geometry. The Hamiltonian contains the creation (annihilation) operator $\hat{a}_i^\dagger$ ($\hat{a}_i$) and the number operator $\hat{n}_i = \hat{a}_i^\dagger \hat{a}_i$ at site i. Equation (1) describes a system with a fixed number N of bosons distributed over M sites, giving a filling factor $\rho = N/M$.

For the ladder lattice geometry considered in this work, $\mathbf{J}$ is characterized by two parameters, J and $J_\perp$, which connect neighboring sites [Fig. 1(a)]. The intrachain hopping rate J describes tunneling between neighboring sites along the same leg of the ladder, while $J_\perp$ denotes the interchain (rung) hopping rate, connecting sites on opposite legs of a rung. The RMI phase has been predicted for a half-filled ($\rho = 1/2$) ladder of HCBs and is characterized by each boson being delocalized over the two sites making up a rung. With the hard-core constraint, the RMI emerges as soon as $J_\perp \neq 0$, but becomes more easily visible when $J_\perp \geqslant J$ [34].

Another way the RMI can be described is by imagining each rung making up a single site of a 1D BH chain. As $J_\perp$ increases, the sites making up the rungs become more and more correlated, delocalizing the population over the rungs, which can then be treated as the single site of a 1D chain [Fig. 1(b)]. This only works for $\rho \leqslant 1/2$, as higher densities imply that bosons share the same rung, becoming impossible to map onto a 1D chain in the HCB limit, which allows only one boson per site. This picture is useful in demonstrating the influence of population density and lattice geometry on insulating phases, suggesting that similar MI phases appear in different quasi-1D ladder lattice geometries.

A. The SF-to-RMI transition for soft-core bosons

The full phase diagrams for the ladder lattice at $\rho = 1/2$ and $L = 40$ were calculated using the density matrix renormalization group (DMRG) [54–56] algorithm as implemented in the ITENSOR library [57,58]. The matrix product operators were constructed by labeling the lattice sites sequentially along the rungs [Fig. 1(a)]. The DMRG calculation performs 150 sweeps to obtain the ground state and 250 sweeps for the first excited state. Singular values smaller than 10^{-8} were discarded, and the maximum occupation number per site was limited to 6. This routine returns the ground-state and first-excited-state eigenenergies E_{GS} and E_{e1} and the single-particle density matrix $\mathbf{p}$ with elements $p_{ij} = \langle \hat{a}_i^\dagger \hat{a}_j \rangle$, which allows us to calculate all observables of interest. For simplicity, we use $J = 1$ as our unit of energy so that the parameters of the model are dimensionless.

The opening of the energy gap $\Delta E = E_{\mathrm{e1}} - E_{\mathrm{GS}}$ occurs for $U/J \gtrsim 10$ and $J_\perp/J \gtrsim 1$, signifying the presence of the RMI phase [Fig. 2(a)]. As U is reduced, the BH model enters the SF phase [30]. Hopping along the chains of the ladder is favored if $J_\perp$ is not strong enough, resulting in delocalization and the emergence of a SF phase.

Although experimentally complex to measure, the mass gap helps visualize when the system enters an insulating phase. To support the observation of a SF-to-RMI transition, we evaluate the hopping correlation function as the average of all the p_{ij} terms which share the same separation d,

$$\Gamma(d) = \frac{\sum_{|\mathbf{x}_i - \mathbf{x}_j| = da} p_{ij}}{\sum_{|\mathbf{x}_i - \mathbf{x}_j| = da} 1}, \tag{2}$$

where d is expressed in units of lattice spacing a. We introduce the correlation functions $\Gamma_{\mathrm{rung}}(d)$ and $\Gamma_{\mathrm{chain}}(d)$, which are defined in the same way as $\Gamma(d)$, but include only terms which link the sites within a rung and a chain, respectively.

For $U/J = 1$ and $J_\perp/J = 15$, we find that $\Gamma_{\mathrm{chain}}(d)$ decays slowly following a power law, with a rapid decay at large d [Fig. 2(c)] due to the open boundary conditions [59]. The

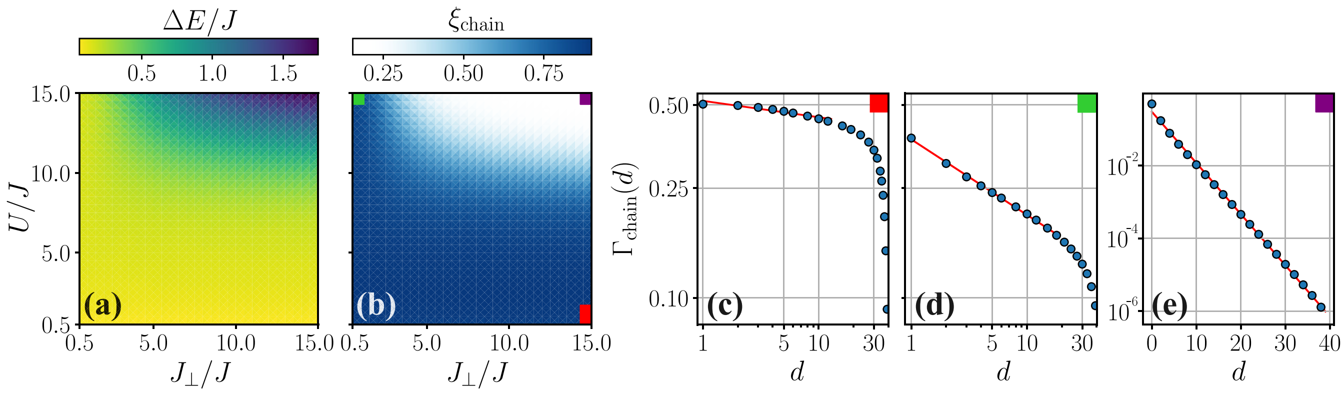

FIG. 2. Phase diagrams showing (a) the energy gap ΔE and (b) the normalized correlation length ξ_{chain} along the chains for a ladder with $\rho = 0.5$ and $L = 40$. The hopping correlation function $\Gamma_{\mathrm{chain}}(d)$ for (c) $U/J = 1$ and $J_\perp/J = 15$, (d) $U/J = 15$ and $J_\perp/J = 0.5$, and (e) $U/J = J_\perp/J = 15$ is also shown. The colored markers show the location of these parameters in the phase diagram of (b). The red line accompanying the data points are fits to (c), (d) power-law and (e) exponential decays. The fitting procedure is detailed in Appendix A.

strong correlations and noticeable influence of the boundary conditions signal the system is in a SF phase. This still holds true for $U/J = 15$ and $J_\perp/J = 0.5$, although $\Gamma_{\mathrm{chain}}(d)$ decays faster than in the previous case [Fig. 2(d)]. On the other hand, if $U/J = J_\perp/J = 15$, then $\Gamma_{\mathrm{chain}}(d)$ decays exponentially [Fig. 2(e)]. We show fits to the data as red solid lines in Fig. 2. In Appendix A we describe the fitting procedure in detail. This change from a power law to an exponential decay is evidence of a Berezinskii-Kosterlitz-Thouless (BKT)–type phase transition into an insulating phase [59].

As shown in Table I, the sets of parameters corresponding to Figs. 2(c) and 2(e) show a constant $\Gamma_{\mathrm{rung}}(d)$, meaning the two chains of the ladder are strongly correlated with each other. A consequence of the exponential decay of $\Gamma_{\mathrm{chain}}(d)$ and constant $\Gamma_{\mathrm{rung}}(d)$ is that each particle is strongly localized to a single rung while at the same time delocalized over its two sites. This is the hallmark of the RMI phase which can also be observed in the population density distribution [Fig. 4(a)], where each boson occupies exactly one rung. Table I also shows $\Gamma_{\mathrm{rung}}(1)$ decreasing in the $J_\perp \to 0$ limit, as in this case the chains are only very weakly coupled.

The different phases can also be distinguished by the correlation length of the system, which is defined as [30]

$$\xi^2 = \frac{1}{\mathcal{N}} \frac{\sum_{d=0} d^2 \Gamma(d)}{\sum_{d=0} \Gamma(d)}. \tag{3}$$

The correlation length is normalized to lie between 0 and 1 by the prefactor $\mathcal{N}$. The maximum correlation length corresponds to a pure SF, where each site is maximally correlated to every other site, and $\Gamma(d)$ is constant. From Eq. (3), two

TABLE I. Hopping correlation function $\Gamma_{\mathrm{rung}}(d)$ along the rungs. The colored markers are used to refer to each set of parameters for the points and graphs highlighted in Fig. 2.

Figure	U/J	$J_\perp/J$	$\Gamma_{\mathrm{rung}}(0)$	$\Gamma_{\mathrm{rung}}(1)$
2(c) ■	1	15	0.500	0.500
2(d) ■	15	0.5	0.500	0.338
2(e) ■	15	15	0.500	0.498

correlation lengths ξ_{chain} and ξ_{rung} can be derived, measuring the decay of correlations along the chains and rungs, respectively. The corresponding normalization factors are $\mathcal{N}_{\mathrm{chain}} = (2L-1)(L-1)/6$ and $\mathcal{N}_{\mathrm{rung}} = 1/2$.

We observe that ξ_{chain} decreases towards 0 as ΔE increases [Fig. 2(b)]. The behavior we observed for finite-size systems is indicative of the existence of a SF-to-RMI BKT-type phase transition for soft-core bosons [60]. We calculate the location of the transition in the thermodynamic limit via scaling analysis [33,61]. More details on the scaling procedure can be found in Appendix B.

The numerical data show the critical value of the on-site interaction U_c/J converging to a finite fixed value when $J_\perp/J \to \infty$. An analytical approximation for large $J_\perp/J$ describing the SF-to-RMI critical boundary is given by [34,62,63]

$$\frac{J_{\perp,c}}{J} \approx A \exp\left(\frac{\pi}{4B\sqrt{U_c/2U_c^{\mathrm{1D}} - 1}}\right), \tag{4}$$

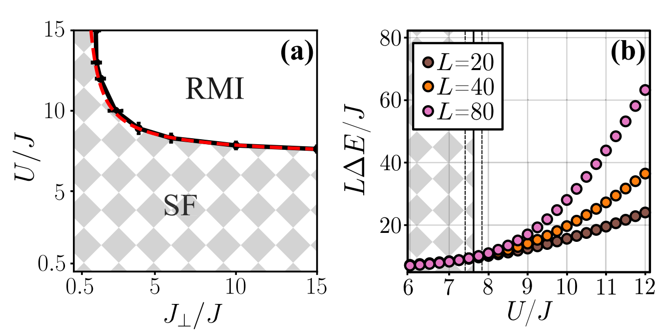

FIG. 3. (a) Phase diagram in the thermodynamic limit for the half-filled ladder lattice. The RMI (white) and SF (checkered) phases are highlighted. The phase boundary (black solid line) includes error bars showing the deviation from results obtained with a more lenient cutoff (see Appendix B). The approximate boundary from Eq. (4) is shown as a red dashed line. (b) Example scaling analysis for $J_\perp/J = 15$. The critical point was derived by comparing the data for different values of L. The extracted value is marked with a black vertical line, while the black dashed borders display the error in this estimate.

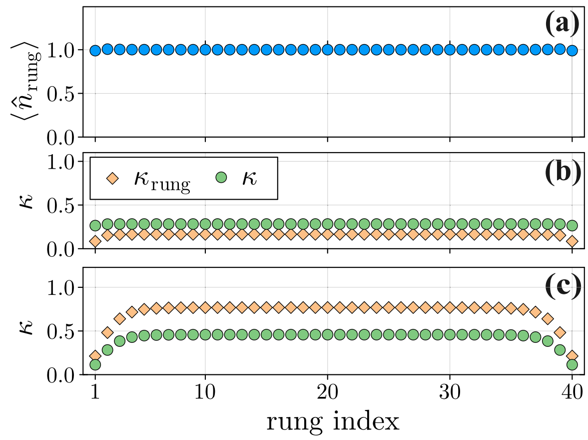

FIG. 4. (a) Population density $\langle \hat{n}_{\rm rung} \rangle$ and (b) corresponding population variances κ and $\kappa_{\rm rung}$ for $U/J = J_\perp/J = 15$. The value of κ is calculated using only the first chain. (c) Population variances for $U/J = 1$ and $J_\perp/J = 15$.

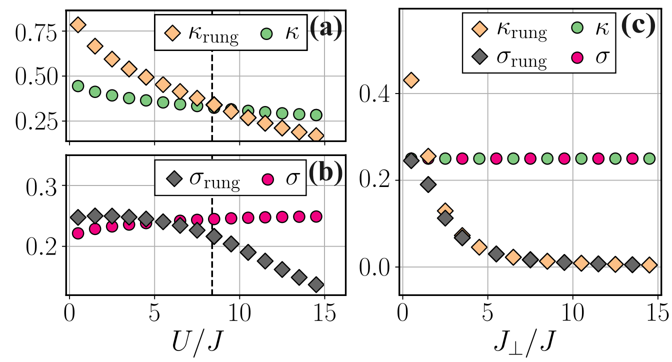

FIG. 5. Average on-site and rung (a) number variances κ and $\kappa_{\rm rung}$ along with (b) the corresponding parity variances σ and $\sigma_{\rm rung}$ calculated for a half-filled ladder ($L = 40$) at $J_\perp/J = 10$. The black dashed line is located at the critical point, calculated via scaling analysis. (c) Same quantities in the HCB limit, where the on-site variances become identical, while the rung variances are distinguishable for $J_\perp \lesssim 4J$.

where A and B are fitting constants and $U_c^{\rm 1D} = 3.25J$ is the critical point for the BH model on a 1D chain at commensurate filling [64]. A brief discussion on how the results from Refs. [34,62,63] were adapted to obtain this equation for our system is given in Appendix C. Fitting the extrapolated numerical data with Eq. (4) gives $A = 0.235$ and $B = 0.457$, showing good agreement across the whole phase diagram, even when $J_\perp$ approaches J [Fig. 3(a)].

The expression in Eq. (4) shows that the critical hopping rate $J_{\perp,c}$ diverges when the on-site interaction approaches $2U_c^{\rm 1D}$, with no phase transition possible for lower U. Hence, the critical on-site interaction for a ladder with infinitely strong $J_\perp$ is equal to $2U_c^{\rm 1D}$. This matches the fact that the rungs act as single sites on a 1D chain for strong enough $J_\perp$.

B. Number and parity variances

We are able to distinguish between the different phases present in the model by using the on-site and rung number variances κ and $\kappa_{\rm rung}$, defined as

$$\kappa = \frac{1}{M}\sum_{l,i}^{M} \langle \hat{n}_{l,i}^2 \rangle - \langle \hat{n}_{l,i} \rangle^2, \tag{5}$$

$$\kappa_{\rm rung} = \frac{1}{L}\sum_{i}^{L} \langle \hat{n}_{{\rm rung},i}^2 \rangle - \langle \hat{n}_{{\rm rung},i} \rangle^2, \tag{6}$$

where $\hat{n}_{l,i}$ is the number operator acting on the site of the ith rung and lth chain, and $\hat{n}_{{\rm rung},i} = \hat{n}_{1,i} + \hat{n}_{2,i}$ is the number operator for said rung. The change in labeling convention is to simplify reading for the ladder case. The convention used in Fig. 1 can be reobtained with $(l, i) \rightarrow j = [4i - 1 + (-1)^l]/2$. These parameters can be interpreted as indicators of the population delocalization, with $\kappa_{\rm rung}$ treating each rung as a single site and therefore only quantifying contributions from the correlations along the chains.

As the interaction strength is increased towards the HCB limit, κ approaches $1/4$, as in this limit the on-site population is reduced to either 0 or 1, while $\kappa_{\rm rung}$ approaches 0 [Figs. 4(b) and 4(c)]. For $J_\perp \rightarrow 0$, the RMI phase has a slow opening of the gap such that $\Delta E/J < 10^{-2}$ before growing substantially in the $1 < J_\perp/J < 2$ regime, even in the HCB limit [34]. This regime is characterized by $\langle \hat{n}_{1,i}\hat{n}_{2,i} \rangle \approx 1/4$, leading to $\kappa_{\rm rung} \approx 1/2$. If $\kappa_{\rm rung}$ is large, so is the rung population variance, which means the bosons on each rung are more likely to be delocalized along the chains, as expected for a SF phase. As κ increases, it is still bounded between $1/4$ and $1/2$, while $\kappa_{\rm rung}$ ranges from 0 to 1. Comparing the values of κ and $\kappa_{\rm rung}$ allows us to approximately determine if the system is in the SF phase, where $\kappa < \kappa_{\rm rung}$, or the RMI phase, where $\kappa > \kappa_{\rm rung}$.

Most quantum-gas microscope experiments only measure the parity of the atom number on each site, as doubly occupied sites are detected as empty due to light-assisted collisions. We now verify how such a parity projection influences the variances discussed above. We define the parity operator at each site [32]

$$\hat{s}_{i,j} = \frac{1 - (-1)^{\hat{n}_{i,j}}}{2}, \tag{7}$$

which is 0 if the population is even and 1 if it is odd. From this we can define the rung parity operator

$$\hat{s}_{{\rm rung},j} = \hat{s}_{1,j} + \hat{s}_{2,j} - 2\hat{s}_{1,j}\hat{s}_{2,j}. \tag{8}$$

The on-site and rung parity variances are defined analogously to Eqs. (5) and (6) and using $\hat{s}_{i,j}$ and $\hat{s}_{{\rm rung},j}$ instead of $\hat{n}_{i,j}$ and $\hat{n}_{{\rm rung},j}$. The average parity variances are defined as

$$\sigma = S(1 - S), \quad \sigma_{\rm rung} = S_{\rm rung}(1 - S_{\rm rung}), \tag{9}$$

where S and $S_{\rm rung}$ are the average on-site and rung parities

$$S = \frac{1}{M}\sum_{l,j}^{M} \langle \hat{s}_{l,j} \rangle, \quad S_{\rm rung} = \frac{1}{L}\sum_{j}^{L} \langle \hat{s}_{{\rm rung},j} \rangle. \tag{10}$$

While for most of the phase diagram κ and σ show similar behaviors, differences arise for small U. As U increases, the on-site parity variance σ increases towards $1/4$, while κ decreases towards it instead [Figs. 5(a) and 5(b)]. This is in line with the average on-site parity being 1/2 in the RMI phase due to the half-filling condition. On the other hand, $\sigma_{\rm rung}$ decays

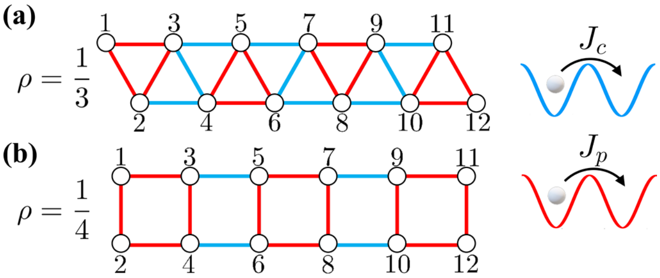

FIG. 6. Lattice geometries of the (a) triangular ladder and (b) square ladder. The J_c (J_p) hopping rate couples the sites connected by blue (red) lines.

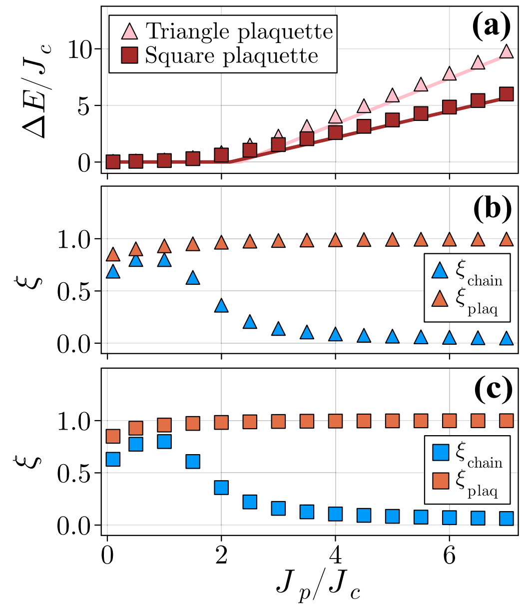

FIG. 7. Phase transition in the triangular ($\rho = 1/3$) and square ($\rho = 1/4$) plaquette ladders, both of size $L = 42$. (a) Energy gap $\Delta E/J_c$. The numerical results (symbols) are compared to analytic result (solid lines) described in the text. The normalized correlation lengths $\xi_{\rm chain}$ and $\xi_{\rm plaq}$ are shown for (b) the triangular plaquette ladder and (c) the square plaquette ladder.

together with $\kappa_{\rm rung}$, mirroring the behavior of population variances for a 1D chain. The variation of $\sigma_{\rm rung}$ across the phase diagram provides an experimentally accessible probe of the different physical behaviors in the SF and RMI phases. The differences between κ and $\kappa_{\rm rung}$ when compared to σ and $\sigma_{\rm rung}$ arise from the contributions of states with highly populated sites. These tend to increase κ and decrease σ because of the inclusion of additional states with even parity.

Since sites with double and higher occupancy are forbidden in the HCB limit, κ and σ are identical and independent of $J_\perp$ [Fig. 5(c)]. Differences emerge when considering the rung-based quantities instead, as both converge and decay towards zero as $J_\perp$ increases but are distinguishable for $J_\perp \to 0$. The difference is explicitly calculated as

$$\kappa_{\rm rung} - \sigma_{\rm rung} = \left(\frac{2}{L}\sum_{i=1}^{L}\langle \hat{n}_{1,i}\hat{n}_{2,i}\rangle\right)^2. \quad (11)$$

The difference between $\kappa_{\rm rung}$ and $\sigma_{\rm rung}$ is related to the average density correlation along the rungs. Hence, an increase in this difference measures an increase of states with doubly occupied rungs. Bosons are then more prone to delocalize over the rungs for small $J_\perp$, although they would not be able to share sites due to the HCB condition.

III. GENERALIZED QUASI-1D GEOMETRIES

The phases observed in the ladder lattice described above include the insulating RMI phase, which requires a density of one particle per rung. This can be attributed to the geometrical properties of the model. Next we investigate whether similar phases arise in two other quasi-1D geometries comparable to the ladder lattice. These are the triangular ladder, which is made up of a chain of triangular plaquettes with population density $\rho = 1/3$, and the square ladder, also referred to as the uniform Su-Schrieffer-Heeger (SSH) ladder [65] and made up of a chain of square plaquettes with population density $\rho = 1/4$. For these the hopping matrix $\mathbf{J}$ is described by two parameters. These are J_c, the hopping rate between sites in different plaquettes, and J_p, the hopping rate between sites within the same plaquette (Fig. 6). We expect the influence of finite on-site interactions on these more complex geometries to be analogous to that of the standard ladder lattice. Thus, we limit our analysis to the HCB case.

To identify the presence of an insulating phase, we again analyze the energy gap ΔE and the correlation length along the chains $\xi_{\rm chain}$. We define the correlation length within a single plaquette $\xi_{\rm plaq}$ as obtained from the plaquette correlation function $\Gamma_{\rm plaq}(d)$, which includes only correlations between sites belonging to the same plaquette. These quantities are calculated in an analogous way to Eqs. (2) and (3). The plaquette correlation length $\xi_{\rm plaq}$ is also normalized as described in Sec. II A.

The relevant BH Hamiltonians were solved via the DMRG method using the same convergence parameters as in the preceding section. We find that the energy gap ΔE opens in a similar way to the standard ladder geometry and is linear in J_p when $J_p \gg J_c$ [Fig. 7(a)]. The gap of the square plaquette ladder opens more slowly than in the triangular ladder. This is contrary to naive expectations from the ladder geometry. The triangular plaquettes are more densely connected, with more hopping paths between neighboring plaquettes than the square ladder. This increased number of connections could make the opening of the energy gap less favorable. However, the triangular plaquettes are also completely connected such that a boson can directly hop between all the sites making up a plaquette. This effect dominates and makes the gap in the triangular ladder open more quickly than in the square ladder.

By calculating ΔE perturbatively for $J_c \ll J_p$, the energy gap of ladders of completely connected plaquettes, such as the triangular ladder, approaches the free-fermion limit (Appendix D)

$$\Delta E = 2J_p - 2\left(\frac{3m-2}{m^2}\right)CJ_c + O\left(J_c^2\right). \quad (12)$$

Here m is the number of sites per plaquette and C the number of connections between a pair of plaquettes. This expansion gets more precise deeper in the insulating regime, where

$J_p/J_c \gg 1$. In this limit, completely connected plaquettes map onto single sites of a 1D chain. To zeroth order, the energy gap opens as $2J_p$, independently of the system size.

Both the triangular and square plaquette ladders can be described as ladders of rings, where the plaquettes have only nearest-neighbor connections. The energy gap in such a system obeys (Appendix D)

$$\Delta E = 4\left[1 - \cos\left(\frac{\pi}{m}\right)\right]J_p - 2\left(\frac{3m-2}{m^2}\right)CJ_c + O\big(J_c^2\big). \tag{13}$$

Plaquettes that are not fully connected, such as in the square ladder, show a weaker influence of J_p and a slower opening of the energy gap. For ladders of plaquettes with equal m, Eq. (13) provides a lower bound for the energy gap. The dependence of ΔE on J_p becomes weaker as plaquette size increases, progressively reducing its contribution. The first-order term of the expansion does not rely on the complete connection condition and is thus more general. This term depends linearly on C but decreases with increasing m. Since it only depends on J_c, it functions as the offset of $\Delta E/J_c$, determining when the gap opens.

The opening of the gap is accompanied by a decay of ξ_{chain} for both geometries [Figs. 7(b) and 7(c)]. These features are especially evident around $J_p = J_c$, where the gap opens more significantly. The correlation length ξ_{chain} increases slightly at small J_p, as hopping along the chains is partly controlled by J_p in both models. Nonetheless, both ΔE and ξ_{chain} show the emergence of an insulating phase. On the other hand, ξ_{plaq} does not decay with increasing J_p; instead it quickly saturates to its maximum value for both geometries. This means that, just like in the standard ladder geometry, the MI phase consists of a single boson localized on each plaquette but delocalized over the sites making up that plaquette. For the chosen densities, this results in there being exactly one boson per plaquette. This is backed up by previous studies for the SSH ladder [65], where an insulating phase was also defined in a similar way. Thus, a plaquette-Mott insulator is observed for these generalized quasi-1D ladder geometries. The RMI is the special case for the standard ladder lattice.

Here we have only examined the case where the density is $\rho = 1/m$. However, equivalent insulating phases also emerge at different densities. The triangular ladder shows such phases for $\rho = 2/3$ due to particle-hole symmetry, and the square ladder reverts to the RMI phase for $\rho = 1/2$ [65]. We also expect insulating phases for the fully filled case, with the largest energy gaps. This was already confirmed with the standard ladder, where a BKT-type transition was observed for the MI-to-SF transition with $\rho = 1$ [33]. Thus, the plaquette-Mott insulator can always be observed when the total number of bosons is an integer multiple of m.

IV. CONCLUSION

In this work we investigated the emergence of the RMI phase in a half-filled bosonic ladder with finite on-site interactions, examined the phase diagram, and characterized the SF-to-RMI transition. We calculated observables such as the on-site and rung variances, which can be directly measured with a quantum-gas microscope [48]. Generalizing the ladder structure showed that a plaquette-Mott insulator can be found in quasi-1D lattices. This insulating phase arises for fractional fillings due to their commensurability with the plaquette size. The lattice structures required for both the triangular [42] and square [41] plaquettes studied here have already been realized experimentally. Similarly, additional insulating phases have been predicted for multileg ladders, where Mott-like phases persist at fillings corresponding to one particle per rung [66–68]. Although increasing the number of legs reduces the energy gap, RMI-like phases should be observable in ladders with a few coupled chains.

Future studies may include a more detailed investigation of commensurability effects at different fillings, as well as the influence of disorder in different lattice structures and densities, which would provide further insight into geometry-induced localization. This would allow an investigation of the commensurate-incommensurate transition in quasi-1D systems and how this physics can influence the MI-to-SF transition.

In addition, ladder lattices continue to serve as a valuable platform to investigate topological effects [69,70]. This leads to the interesting possibility of using them to study both dynamics-induced [71] and interaction-induced [65,72] topological physics. Quasi-1D geometries can also provide insights into the physics of mobile impurities interacting with a bath [73,74]. The ladder lattice has already been used to theoretically investigate the influence of dimensionality on the Anderson orthogonality catastrophe [75]. Generalizing these ideas to more involved quasi-1D geometries may lead to the emergence of novel dynamical features.

Finally, the ladder has been useful for studying the crossover between different dimensionalities [10–12,68]. This characteristic was used to observe the emergence of 2D physics from a 1D structure. Studying these effects using fractal geometries, which have a fractional dimensionality [76–78], creates an opportunity for studying the stability of the RMI and related states to disorder arising from both the Hamiltonian and the lattice geometry.

ACKNOWLEDGMENTS

We thank Arthur La Rooij, Christopher Parsonage, and Lennart Koehn for helpful discussions. This work was supported by the Engineering and Physical Sciences Research Council: L.C. through the Doctoral Training Partnership (Grant No. EP/W524670/1), S.K. through the program "Quantum advantage in quantitative quantum simulation" (Grant No. EP/Y01510X/1), and P.K. through Grant No. EP/Z533713/1.

DATA AVAILABILITY

The data used in this work are openly available [79].

APPENDIX A: FITTING THE DECAY OF $\Gamma_{\text{chain}}(d)$

In this appendix we describe our fitting procedure for both the power-law and exponential decay of $\Gamma_{\text{chain}}(d)$ in the RMI and SF regimes for an $L = 40$ half-filled ladder, as shown in Fig. 2. In the SF regime, we expect $\Gamma_{\text{chain}}(d)$ to follow a power-law decay $\Gamma_{\text{chain}}(d) = cd^{-k}$ [59]. We performed a

TABLE II. Functions and parameters describing the fitting of $\Gamma_{\text{chain}}(d)$ shown as red lines in Fig. 2. The colored markers are used to refer to each set of parameters for the points and graphs highlighted in Fig. 2.

Figure	$\Gamma_{\text{chain}}(d)$	k	$\ln c$
2(c) ■	cd^{-k}	0.066	−0.656
2(d) ■	cd^{-k}	0.273	−0.981
2(e) ■	ce^{-kd}	0.324	−1.193

linear fit in the log-log scale to extract both the gradient k and intercept $\ln c$. Since the boundary conditions influence the decay of $\Gamma_{\text{chain}}(d)$ when d is close to the system size, we only fitted to the data for $1 \leqslant d \leqslant 20$.

We expect an exponential decay $\Gamma_{\text{chain}}(d) = ce^{-kd}$ in the insulating phase [59] [see Fig. 2(e)]. In this case we were able to fit $\Gamma_{\text{chain}}(d)$ over all data points $1 \leqslant d \leqslant 40$. These fits are shown as red lines in Figs. 2(c)–2(e). The parameters obtained from the fitting are shown in Table II. In the SF phase, the decay rate is very small [see Fig. 2(c)]. The power law decays much more quickly for larger U [Fig. 2(d)] since the parameters are closer the RMI phase boundary.

As predicted by the Luttinger liquid picture, the correlation functions in the SF phase are described by a scaling law proportional to $d^{-1/4K_s}$, where K_s is the symmetric Luttinger liquid parameter [18,34]. We find $K_s \approx 0.91$ for the parameters in Fig. 2(d) slightly away from the value $K_s = 1$ expected at the critical point. This is both because the parameters used are not at the critical point and due to finite-size effects.

APPENDIX B: SCALING ANALYSIS

Here we discuss the scaling analysis approach we used to determine the location of the SF-to-RMI transition [33,61]. A useful indication of this transition is the change in behavior of the correlation function from a power-law decay in the SF to exponential decay in an insulating phase. The SF-to-RMI phase transition belongs to the BKT universality class and is therefore properly defined in the thermodynamic limit where $M \to \infty$ and ρ remains finite.

We used the finite-size scaling analysis close to the critical region to calculate the energy gap, which follows the standard scaling function [80]

$$\Delta E \approx \frac{1}{L} f\left(\frac{L}{\xi_{\text{chain}}}\right), \tag{B1}$$

where $f(x)$ is constant when $x \ll 1$. Consequently, different curves for different values of $L\Delta E/J$ converge in the SF phase and diverge in an insulating phase.

We computed curves for $L = 20, 40, 80$ using the DMRG method with a cutoff of 10^{-8} and derived transition points by varying U at fixed $J_\perp$ and vice versa. Given the increasing sizes of the matrix product operators, the number of singular-value decomposition sweeps of both the ground and first excited states, $|\text{GS}\rangle$ and $|\text{e1}\rangle$ respectively, were increased with system size (Table III). We consider the curves as converged when the difference between $L\Delta E/J$ of different system sizes is less than 5×10^{-3}. The standard error was calculated following a similar procedure and by imposing a more lenient

TABLE III. Number of sweeps imposed to converge with the DMRG method to the ground state $|\text{GS}\rangle$ and first excited state $|\text{e1}\rangle$ for different sizes L. The retrieved matrix product states were used for scaling analysis and calculation of the Roomany-Wyld approximant.

State	$L = 20$	$L = 39, 40$	$L = 80$
$\|\text{GS}\rangle$	60	150	180
$\|\text{e1}\rangle$	150	250	250

cutoff of 10^{-2} [see Fig. 3(a) for main results and Fig. 3(b) for an example of $L\Delta E/J$ versus U and $J_\perp/J = 15$].

To further confirm that the phase transition for the ladder is of BKT type, we use the Roomany-Wyld approximant of the β function [61,81]

$$\beta_{LL'}(g) = \frac{1 - \ln[\xi_{\text{chain}}(L)/\xi_{\text{chain}}(L')]/\ln(L/L')}{\sqrt{\xi_{\text{chain}}(L)\xi_{\text{chain}}(L')/\xi'_{\text{chain}}(L)\xi'_{\text{chain}}(L')}}, \tag{B2}$$

where $\xi'_{\text{chain}}(L) = \partial\xi_{\text{chain}}(L)/\partial g$ and g is a parameter influencing the system, with either $g = U$ or $g = J_\perp$. For Eq. (B2) to be valid, the chain lengths L and L' must be as close as possible, and we chose $L = 40$ and $L' = 39$.

For a BKT-type transition, it has been shown that Eq. (B2) reduces to $\beta_{\text{BKT}}(g) = G(g - g_c)^{1+\gamma}$ close to the transition point at g_c, with the critical exponent $\gamma = 0.5$ [81] and G as a free scaling constant. We verify the BKT nature of the phase transition by fitting β_{BKT} to the calculated values of $\beta_{LL'}$ versus U [Fig. 8(a)] and $J_\perp$ [Fig. 8(b)].

By performing this fit, the critical point was found to be $U_c^{\text{RW}}/J = 7.98$ for $J_\perp/J = 15$, while Eq. (4) returns the critical value $U_c^a/J = 7.61$, with a relative error between the two of $\delta_U = |U_c^{\text{RW}} - U_c^a|/J = 0.37$. For $U/J = 15$, we obtained the critical value via fitting to be $J_{\perp,c}^{\text{RW}}/J = 1.31$, while Eq. (4) gives $J_{\perp,c}^a/J = 1.06$, with a relative error between the two of $\delta_J = |J_{\perp,c}^{\text{RW}} - J_{\perp,c}^a|/J = 0.25$.

APPENDIX C: CALCULATING THE PHASE BOUNDARIES

We discuss here how the work from Refs. [34,62,63] was applied to obtain Eq. (4). We start by considering the renormalization group (RG) flow equations from Eqs. (3.18) and (3.19) in Ref. [34] for correlated chains. The

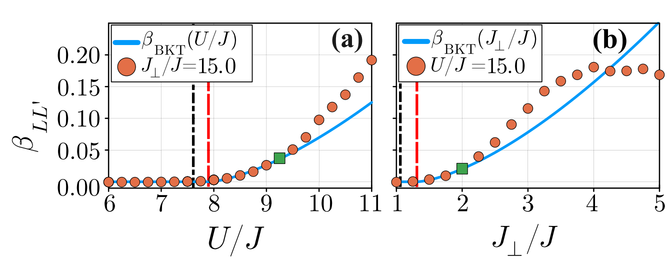

FIG. 8. Numerical results of $\beta_{LL'}$ [Eq. (B2)] (a) vs U for fixed $J_\perp/J = 15$ and (b) vs $J_\perp$ for fixed $U/J = 15$. Blue lines are a fit with β_{BKT}, and the green squares are the last points used in the fitting routine. The black dot-dashed line locates the critical point calculated using Eq. (4), while the red dashed line locates the critical point retrieved by fitting β_{BKT} to the $\beta_{LL'}$ data.

equations were derived by applying bosonization, resulting in a Hamiltonian depending on the symmetric (antisymmetric) Luttinger parameter $K_{s(a)}$ and group velocity v. The RG flow equations were obtained by defining four dimensionless coupling parameters: the antisymmetric y_a, symmetric y_s, and interchain $y_\perp$ couplings, along with g_s, which is generated under RG flow. These coupling parameters are read as $y_\perp(a) = aJ_\perp/v$, $y_a(a) = y_s(a) = aJ_\perp v$, and $g_s(a) = 0$, with a the lattice periodicity.

Following Ref. [34], we introduce $\tilde{K}_s = K_s(l_\perp)$ and $\tilde{g}_s(l_\perp) = g_s(l_\perp) + 2\eta y_s(l_\perp)$, where $l_\perp$ is a scale such that $y_\perp(l_\perp) = 1$. For low-energy scales, the RG equations are

$$\frac{d\tilde{g}_s}{dl} = (2 - 2\tilde{K}_s)\tilde{g}_s, \tag{C1}$$

$$\frac{d\tilde{K}_s}{dl} = -2\tilde{g}_s^2\tilde{K}_s^2, \tag{C2}$$

where the flow parameter is defined as $l = \ln\tilde{a}(l)$, with $\tilde{a}(l) = a(l)/a$ the unitless characteristic length scale $a(l)$. The low-energy scale is defined in the region of $l > l_\perp$. This is analogous to describing the region where the tunneling along the chain is weak compared to that along the rungs, $J \ll J_\perp$.

Following these equations, the RG transformation drives the coupling $\tilde{g}_s$ towards strong coupling, leading to a gap opening. Following the analysis done in previous works [63], defining $\tilde{K}_n = 1/2\tilde{K}_s$ leads to

$$\frac{d\tilde{g}_s}{dl} = \left(2 - \frac{1}{\tilde{K}_n}\right)\tilde{g}_s, \tag{C3}$$

$$\frac{d\tilde{K}_n}{dl} = \tilde{g}_s^2, \tag{C4}$$

which are the sine-Gordon equations for the purely commensurate gapped phase [62] of weakly coupled rungs. Strengthening the coupling between the rungs would bring the system outside the gapped region after some crossover scale l_*. The relationship between $J/J_\perp$ and the length scale $\tilde{a}(l)$ is defined as

$$J/J_\perp \propto \tilde{a}(l)^{-s}. \tag{C5}$$

As we approach l_* from the gapped side, $\tilde{K}_n$ can be written as [62,63]

$$\tilde{K}_n = \frac{1}{2} + \mathcal{A}\tan\left(4\mathcal{A}l - \frac{\pi}{2}\right), \tag{C6}$$

where $\mathcal{A} \propto \sqrt{U/U_0 - 1}$ and the parameter U_0 is the critical transition point for the case of $J/J_\perp \to 0$. From this equation we can see that $K_n(l) \approx 1/2$ until it diverges as l approaches $\pi/4\mathcal{A}$. Hence, $l_* = \pi/4\mathcal{A}$ determines the transition from the MI to the SF phase via rung coupling. The critical boundary then behaves as

$$\frac{(J_\perp)_c}{J} \propto \exp\left(\frac{\pi s}{4b\sqrt{U/U_0 - 1}}\right), \tag{C7}$$

where s and b are scaling constants. We note the value s can be absorbed by the constant b as $B = b/s$.

Since we use $J = 1$ for all our calculations, we define U_0 as the transition point as $J_\perp \to \infty$. To determine U_0, we consider the energy gap ΔE for an increasingly strong perpendicular hopping. The results show how the ΔE of a $\rho = 0.5$ ladder converges to the behavior of the ΔE of a $\rho = 1$ chain with $2J$ hopping as $J_\perp \to \infty$ (Fig. 9). This makes intuitive sense, as we would expect $U_0 = 2U_c^{1D}$ due to the existence of two tunneling connections when looking at intrarung hopping. Thus, the SF-to-RMI boundary transition follows Eq. (4).

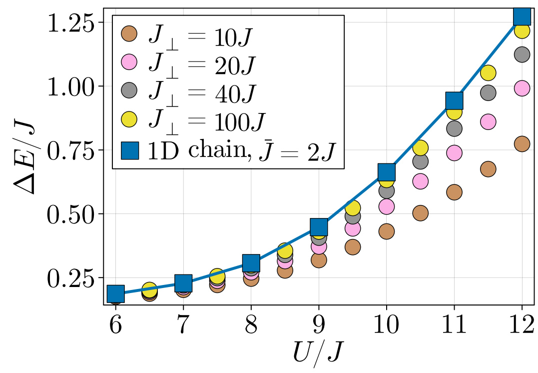

FIG. 9. Energy gap of a half-filled ladder lattice vs interaction strength for different values of $J_\perp$ (circles), compared to a 1D chain with an effective hopping parameter of $2J$ (squares). The line is to guide the eye.

APPENDIX D: LINEAR LIMIT OF THE HCB MASS GAP FOR GENERALIZED LADDERS

To explain the derivation of the energy gaps for completely connected and ring plaquettes [Eqs. (12) and (13)], we use perturbation theory [82] and follow the approach of Ref. [34]. While our numerical simulations calculate $\Delta E = E_{\rm e1} - E_{\rm GS}$, Ref. [34] uses the charge gap, defined as $\Delta E = \epsilon(L+1) + \epsilon(L-1) - 2\epsilon(L)$, where $\epsilon(N) = E_{\rm GS}(N)$ is the ground state for N bosons. However, for the SF-to-RMI transition, these quantities have the same behavior in the thermodynamic limit. We consider a chain of plaquettes, each made up of m sites and n bosons. In the HCB limit, the Hamiltonian is $\hat{H} = -J_p\hat{H}_{\rm plaq} - J_c\hat{H}_{\rm conn}$, where $H_{\rm plaq}$ defines the intraplaquette connections and $H_{\rm conn}$ the interplaquette ones. We define the energy of a single plaquette with n bosons on m sites as $E_{n,m}$.

1. Completely connected plaquettes

In the following, we discuss the derivation of the charge gap of ladders of completely connected plaquettes [Eq. (12)]. To calculate the zeroth order, we consider only a single plaquette. In this case, the $\hat{H}_{\rm plaq}$ matrix spans a Hilbert space of dimension $d(n,m) = m!/n!(m-n)!$, with each row containing $n(m-n)$ nonzero elements, as each boson can hop to any unoccupied site. Thus, the lowest eigenenergy is $E_{n,m} = -J_pn(m-n)$, with ground state $|n\rangle$.

The ground state of a chain of L_p plaquettes and L_p bosons is $|L_p\rangle = |1\rangle \otimes |1\rangle \otimes \cdots \otimes |1\rangle$ with energy $\epsilon^{(0)}(L_p) = L_pE_{1,m} = -J_pL_p(m-1)$. If we consider a chain with $L_p + 1$ bosons, one of the plaquettes must be doubly occupied, and the energy in this case is $\epsilon^{(0)}(L_p+1) = (L_p-1)E_{1,m} + E_{2,m} = -J_p(L_p-1)(m-1) - 2J_p(m-2)$. Similarly, for the case of $L_p - 1$ bosons, one plaquette must be empty, leading to $\epsilon^{(0)}(L_p - 1) = (L_p - 1)E_{1,m} + E_{0,m} = -J_p(L_p - 1)(m-1)$. Hence, the zeroth order of the charge gap is $\Delta E^{(0)} = 2J_p$, independent of the plaquette structure.

2. Ring plaquettes

Here we discuss the derivation of the charge gap for ladders of ring plaquettes [Eq. (13)]. The zeroth-order term is calculated by considering a single ring plaquette, which is treated as a chain with periodic boundary conditions. The ground-state energy is $E_{1,m} = -2J_p$ if one boson is present and $E_{0,m} = 0$ if empty, leading to $\epsilon^{(0)}(L_p) = -2J_pL_p$ and $\epsilon^{(0)}(L_p - 1) = -2J_p(L_p - 1)$. The term $\epsilon^{(0)}(L_p + 1)$ requires the ground-state energy of a chain with periodic boundary conditions and two interacting bosons, $E_{2,m}$. The eigenstate $|\Psi\rangle$ of this system is obtained using the Bethe ansatz [83],

$$|\Psi\rangle = \sum_{x_1,x_2} \Psi(x_1, x_2)|x_1, x_2\rangle, \tag{D1}$$

$$\Psi(x_1, x_2) = A_{12}e^{i(k_1x_1+k_2x_2)} + A_{21}e^{i(k_1x_2+k_2x_1)}, \tag{D2}$$

as defined in the $x_1 \leqslant x_2$ domain, with x_1 and x_2 (k_1 and k_2) the positions (quasimomenta) of the two bosons. By symmetry, the $x_2 \leqslant x_1$ domain is described by $\Psi(x_2, x_1)$ and exchanged quasimomenta. Using this ansatz, the total energy and amplitudes of the system are [83]

$$E_{2,m} = -2J_p[\cos(k_1) + \cos(k_2)], \tag{D3}$$

$$A_{12} = -\left(\sin k_2 + \sin k_1 - i\frac{U}{2J_p}\right), \tag{D4}$$

$$A_{21} = \left(\sin k_1 + \sin k_2 - i\frac{U}{2J_p}\right). \tag{D5}$$

Under periodic boundary conditions, the quasimomenta obey the Bethe ansatz equations,

$$\exp(ik_jm) = \frac{\sin k_l - \sin k_j - iU/2J_p}{\sin k_l - \sin k_j + iU/2J_p}, \tag{D6}$$

with $j \neq l \in [1, 2]$. Imposing the HCB limit $U \to \infty$ leads to $k_j = \pm\pi/m$ and the two quasimomenta being either equal ($k_1 = k_2$) or opposite ($k_1 = -k_2$), with energy $E_{2,m} = -4J_p\cos(\pi/m)$ in both cases.

Thus, the zeroth order of the charge gap of a ring plaquette is $\Delta E^{(0)} = 4[1 - \cos(\pi/m)]J_p$. This solution requires periodic boundary conditions, which only exist for $m \geqslant 3$.

We note that instead of using the Bethe ansatz approach carried out here, this calculation could also have been performed using a Jordan-Wigner transformation, giving the same results as those obtained here.

3. First-order approximation

We now look at the first-order perturbation for small J_c/J_p, induced to $\hat{H}_{\text{plaq}}$ by $\hat{H}_{\text{conn}}$. Since $\hat{H}_{\text{conn}}$ describes interplaquette hopping, applying it on the zeroth order of the ground state $|\text{GS}^{(0)}\rangle$ would result in $2(L_p - 1)$ particle-hole excitations on neighboring plaquettes. The first-order energy approximation for L_p bosons is $\epsilon^{(1)}(L_p) = -J_c\langle L_p|\hat{H}_{\text{plaq}}|L_p\rangle = 0$. However, the first order becomes relevant for $L_p \pm 1$ bosons. In the $L_p + 1$ case, the ground state can be described as the superposition of many degenerate states

$$|\text{GS}^{(0)}(L_p + 1)\rangle = \frac{1}{\sqrt{L_p}}\sum_{j=1}^{L_p} e^{ikj}|2(j)\rangle,$$

with quasimomentum k. We define the state $|2(j)\rangle = |1\rangle \otimes \cdots \otimes |2\rangle_j \otimes \cdots \otimes |1\rangle$, with $L_p - 1$ copies of the $|1\rangle$ state. Up to first order, $\hat{H}_{\text{conn}}$ only contains terms describing the transfer of a boson onto neighboring plaquettes, as higher-order terms would be neglected. Since the interhopping structure is consistent between different pairs of neighboring plaquettes, we define the $\hat{H}_{\text{hop}}$ matrix as connecting the jth plaquette to the $(j+1)$th one, having two and one bosons, respectively. Given this, the Hilbert subspace of $\hat{H}_{\text{hop}}$ is of size $d(1, m)d(2, m) = m^2(m-1)/2$. Defining $|12\rangle = |1\rangle \otimes |2\rangle$ and $|21\rangle = |2\rangle \otimes |1\rangle$, the first-order term becomes

$$\begin{aligned}\epsilon^{(1)}(L_p + 1) &= -J_c\langle \text{GS}^{(0)}(L_p + 1)|\hat{H}_{\text{conn}}|\text{GS}^{(0)}(L_p + 1)\rangle \\ &= -J_c(\langle 21|\hat{H}_{\text{hop}}|12\rangle e^{ik} + \langle 12|\hat{H}_{\text{hop}}|21\rangle e^{-ik}) \\ &= -2S_{\text{hop}}J_c\cos(k),\end{aligned} \tag{D7}$$

where $S_{\text{hop}} = \sum_{i,j}(\hat{H}_{\text{hop}})_{i,j}$ is the sum of all the elements in the $\hat{H}_{\text{hop}}$ matrix.

We obtain $S_{\text{hop}} = C_+/d(1, m)d(2, m)$, where C_+ is the number of possible pairs of states that permit the transfer of a boson from the doubly occupied plaquette j to the singly occupied one $j+1$. For each connection between these plaquettes, there must be a state where one site is occupied by a boson and the other is free. For that connection, there are $m-1$ states depending on the position of the second boson on plaquette j, multiplied by another $m-1$ accounting for the possible sites the boson on plaquette $j+1$ can occupy without blocking the hopping. This gives $C_+ = (m-1)^2C$, where C is the number of interplaquette connections, and the first-order perturbation becomes

$$\epsilon^{(1)}(L_p + 1) = -4J_c\frac{m-1}{m^2}C\cos(k). \tag{D8}$$

The same process is applied for $|\text{GS}^{(0)}(L_p - 1)\rangle$, but instead of $|2(j)\rangle$ we consider $|0(j)\rangle = |1\rangle \otimes \cdots \otimes |0\rangle_j \otimes \cdots \otimes |1\rangle$, with $S_{\text{hop}} = C_-/d(1, m)d(0, m) = C_-/m$. Here C_- is the number of pairs of states that allow for a hole to move from plaquette j to $j+1$. Since we only have one particle for both plaquettes, $C_- = C$. The first-order perturbation is

$$\epsilon^{(0)}(L_p - 1) = -\frac{2C}{m}J_c\cos(k). \tag{D9}$$

Finally, the charge gap up to first order is

$$\begin{aligned}\Delta E^{(1)} &= \epsilon^{(1)}(L_p + 1) + \epsilon^{(1)}(L_p - 1) \\ &= -2J_c\left(\frac{3m-2}{m^2}\right)C.\end{aligned} \tag{D10}$$

By combining the zeroth and first orders of the charge gap, we obtain the results used in the main text in Eqs. (12) and (13).

[1] T. Stöferle, H. Moritz, C. Schori, M. Köhl, and T. Esslinger, Transition from a strongly interacting 1D superfluid to a Mott insulator, Phys. Rev. Lett. **92**, 130403 (2004).

[2] I. Bloch, J. Dalibard, and W. Zwerger, Many-body physics with ultracold gases, Rev. Mod. Phys. **80**, 885 (2008).

[3] C. Gross and I. Bloch, Quantum simulations with ultracold atoms in optical lattices, Science **357**, 995 (2017).

[4] G.-B. Jo, J. Guzman, C. K. Thomas, P. Hosur, A. Vishwanath, and D. M. Stamper-Kurn, Ultracold atoms in a tunable optical kagome lattice, Phys. Rev. Lett. **108**, 045305 (2012).

[5] L. Tarruell, D. Greif, T. Uehlinger, G. Jotzu, and T. Esslinger, Creating, moving and merging Dirac points with a Fermi gas in a tunable honeycomb lattice, Nature (London) **483**, 302 (2012).

[6] M. Aidelsburger, M. Atala, M. Lohse, J. T. Barreiro, B. Paredes, and I. Bloch, Realization of the Hofstadter Hamiltonian with ultracold atoms in optical lattices, Phys. Rev. Lett. **111**, 185301 (2013).

[7] M. Atala, M. Aidelsburger, J. T. Barreiro, D. Abanin, T. Kitagawa, E. Demler, and I. Bloch, Direct measurement of the Zak phase in topological Bloch bands, Nat. Phys. **9**, 795 (2013).

[8] E. J. Meier, F. A. An, and B. Gadway, Observation of the topological soliton state in the Su–Schrieffer–Heeger model, Nat. Commun. **7**, 13986 (2016).

[9] M. Leder, C. Grossert, L. Sitta, M. Genske, A. Rosch, and M. Weitz, Real–space imaging of a topologically protected edge state with ultracold atoms in an amplitude–chirped optical lattice, Nat. Commun. **7**, 13112 (2016).

[10] M. C. Revelle, J. A. Fry, B. A. Olsen, and R. G. Hulet, 1D to 3D crossover of a spin-imbalanced Fermi gas, Phys. Rev. Lett. **117**, 235301 (2016).

[11] H. Yao, L. Pizzino, and T. Giamarchi, Strongly–interacting bosons at 2D–1D dimensional crossover, SciPost Phys. **15**, 050 (2023).

[12] Y. Guo, H. Yao, S. Ramanjanappa, S. Dhar, M. Horvath, L. Pizzino, T. Giamarchi, M. Landini, and H.-C. Nägerl, Observation of the 2D–1D crossover in strongly interacting ultracold bosons, Nat. Phys. **20**, 934 (2024).

[13] M. Cazalilla, Bosonizing one-dimensional cold atomic gases, J. Phys. B **37**, S1 (2004).

[14] M. A. Cazalilla, R. Citro, T. Giamarchi, E. Orignac, and M. Rigol, One dimensional bosons: From condensed matter systems to ultracold gases, Rev. Mod. Phys. **83**, 1405 (2011).

[15] T. Giamarchi, One-dimensional physics in the 21st century, C. R. Phys. **17**, 322 (2016).

[16] A. Vogler, R. Labouvie, G. Barontini, S. Eggert, V. Guarrera, and H. Ott, Dimensional phase transition from an array of 1D Luttinger liquids to a 3D Bose-Einstein condensate, Phys. Rev. Lett. **113**, 215301 (2014).

[17] M. Atala, M. Aidelsburger, M. Lohse, J. T. Barreiro, B. Paredes, and I. Bloch, Observation of chiral currents with ultracold atoms in bosonic ladders, Nat. Phys. **10**, 588 (2014).

[18] P. Donohue and T. Giamarchi, Mott-superfluid transition in bosonic ladders, Phys. Rev. B **63**, 180508(R) (2001).

[19] A. Tokuno and A. Georges, Ground states of a Bose–Hubbard ladder in an artificial magnetic field: Field-theoretical approach, New J. Phys. **16**, 073005 (2014).

[20] M. Piraud, F. Heidrich-Meisner, I. P. McCulloch, S. Greschner, T. Vekua, and U. Schollwöck, Vortex and Meissner phases of strongly interacting bosons on a two-leg ladder, Phys. Rev. B **91**, 140406(R) (2015).

[21] M. Buser, C. Hubig, U. Schollwöck, L. Tarruell, and F. Heidrich-Meisner, Interacting bosonic flux ladders with a synthetic dimension: Ground-state phases and quantum quench dynamics, Phys. Rev. A **102**, 053314 (2020).

[22] A. Petrescu and K. Le Hur, Chiral Mott insulators, Meissner effect, and Laughlin states in quantum ladders, Phys. Rev. B **91**, 054520 (2015).

[23] M. Di Dio, S. De Palo, E. Orignac, R. Citro, and M.-L. Chiofalo, Persisting Meissner state and incommensurate phases of hard-core boson ladders in a flux, Phys. Rev. B **92**, 060506(R) (2015).

[24] E. Orignac, R. Citro, M. Di Dio, S. De Palo, and M.-L. Chiofalo, Incommensurate phases of a bosonic two-leg ladder under a flux, New J. Phys. **18**, 055017 (2016).

[25] A. Impertro, S. Huh, S. Karch, J. F. Wienand, I. Bloch, and M. Aidelsburger, Strongly interacting Meissner phases in large bosonic flux ladders, Nat. Phys. **21**, 895 (2025).

[26] E. Orignac and T. Giamarchi, Meissner effect in a bosonic ladder, Phys. Rev. B **64**, 144515 (2001).

[27] T. Giamarchi, Mott transition in one dimension, Physica B **230–232**, 975 (1997).

[28] M. Greiner, O. Mandel, T. Esslinger, T. W. Hänsch, and I. Bloch, Quantum phase transition from a superfluid to a Mott insulator in a gas of ultracold atoms, Nature (London) **415**, 39 (2002).

[29] D. Jaksch, C. Bruder, J. I. Cirac, C. W. Gardiner, and P. Zoller, Cold bosonic atoms in optical lattices, Phys. Rev. Lett. **81**, 3108 (1998).

[30] T. D. Kühner and H. Monien, Phases of the one-dimensional Bose-Hubbard model, Phys. Rev. B **58**, R14741 (1998).

[31] K. V. Krutitsky, Ultracold bosons with short-range interaction in regular optical lattices, Phys. Rep. **607**, 1 (2016).

[32] A. Di Carli, C. Parsonage, A. La Rooij, L. Koehn, C. Ulm, C. W. Duncan, A. J. Daley, E. Haller, and S. Kuhr, Commensurate and incommensurate 1D interacting quantum systems, Nat. Commun. **15**, 474 (2024).

[33] M. S. Luthra, T. Mishra, R. V. Pai, and B. P. Das, Phase diagram of a bosonic ladder with two coupled chains, Phys. Rev. B **78**, 165104 (2008).

[34] F. Crépin, N. Laflorencie, G. Roux, and P. Simon, Phase diagram of hard-core bosons on clean and disordered two-leg ladders: Mott insulator-Luttinger liquid-Bose glass, Phys. Rev. B **84**, 054517 (2011).

[35] A. Petrescu, M. Piraud, G. Roux, I. P. McCulloch, and K. Le Hur, Precursor of the Laughlin state of hard-core bosons on a two-leg ladder, Phys. Rev. B **96**, 014524 (2017).

[36] M. Girardeau, Relationship between systems of impenetrable bosons and fermions in one dimension, J. Math. Phys. **1**, 516 (1960).

[37] J. Carrasquilla, F. Becca, and M. Fabrizio, Bose-glass, superfluid, and rung-Mott phases of hard-core bosons in disordered two-leg ladders, Phys. Rev. B **83**, 245101 (2011).

[38] A. Padhan, R. Parida, S. Lahiri, M. K. Giri, and T. Mishra, Quantum phases of constrained bosons on a two-leg Bose-Hubbard ladder, Phys. Rev. A **108**, 013316 (2023).

[39] M. Singh, T. Mishra, R. V. Pai, and B. P. Das, Quantum phases of attractive bosons on a Bose-Hubbard ladder with three-body constraint, Phys. Rev. A **90**, 013625 (2014).

[40] A. Keleş and M. O. Oktel, Mott transition in a two-leg Bose-Hubbard ladder under an artificial magnetic field, Phys. Rev. A **91**, 013629 (2015).

[41] Z. Dong, H. Li, H. Wang, Y. Pan, W. Yi, and B. Yan, Observation of higher-order topological bound states in the continuum using ultracold atoms, arXiv:2501.13499.

[42] C. Becker, P. Soltan-Panahi, J. Kronjäger, S. Dörscher, K. Bongs, and K. Sengstock, Ultracold quantum gases in triangular optical lattices, New J. Phys. **12**, 065025 (2010).

[43] W. S. Bakr, J. I. Gillen, A. Peng, S. Fölling, and M. Greiner, A quantum gas microscope for detecting single atoms in a Hubbard-regime optical lattice, Nature (London) **462**, 74 (2009).

[44] J. F. Sherson, C. Weitenberg, M. Endres, M. Cheneau, I. Bloch, and S. Kuhr, Single-atom-resolved fluorescence imaging of an atomic Mott insulator, Nature (London) **467**, 68 (2010).

[45] G. J. A. Edge, R. Anderson, D. Jervis, D. C. McKay, R. Day, S. Trotzky, and J. H. Thywissen, Imaging and addressing of individual fermionic atoms in an optical lattice, Phys. Rev. A **92**, 063406 (2015).

[46] E. Haller, J. Hudson, A. Kelly, D. A. Cotta, B. Peaudecerf, G. D. Bruce, and S. Kuhr, Single-atom imaging of fermions in a quantum-gas microscope, Nat. Phys. **11**, 738 (2015).

[47] S. Kuhr, Quantum-gas microscopes: A new tool for cold-atom quantum simulators, Nat. Sci. Rev. **3**, 170 (2016).

[48] C. Gross and W. S. Bakr, Quantum gas microscopy for single atom and spin detection, Nat. Phys. **17**, 1316 (2021).

[49] P. M. Preiss, R. Ma, M. E. Tai, J. Simon, and M. Greiner, Quantum gas microscopy with spin, atom-number, and multilayer readout, Phys. Rev. A **91**, 041602(R) (2015).

[50] G. Gauthier, I. Lenton, N. McKay Parry, M. Baker, M. Davis, H. Rubinsztein-Dunlop, and T. Neely, Direct imaging of a digital-micromirror device for configurable microscopic optical potentials, Optica **3**, 1136 (2016).

[51] P. Zupancic, P. M. Preiss, R. Ma, A. Lukin, M. E. Tai, M. Rispoli, R. Islam, and M. Greiner, Ultra-precise holographic beam shaping for microscopic quantum control, Opt. Express **24**, 13881 (2016).

[52] J.-y. Choi, S. Hild, J. Zeiher, P. Schauß, A. Rubio-Abadal, T. Yefsah, V. Khemani, D. A. Huse, I. Bloch, and C. Gross, Exploring the many-body localization transition in two dimensions, Science **352**, 1547 (2016).

[53] S. Wili, T. Esslinger, and K. Viebahn, An accordion superlattice for controlling atom separation in optical potentials, New J. Phys. **25**, 033037 (2023).

[54] U. Schollwöck, The density-matrix renormalization group, Rev. Mod. Phys. **77**, 259 (2005).

[55] U. Schollwöck, The density-matrix renormalization group in the age of matrix product states, Ann. Phys. (N.Y.) **326**, 96 (2011).

[56] R. Orús, Tensor networks for complex quantum systems, Nat. Rev. Phys. **1**, 538 (2019).

[57] M. Fishman, S. R. White, and E. M. Stoudenmire, The ITensor software library for tensor network calculations, SciPost Phys. Codebases 4 (2022).

[58] M. Fishman, S. R. White, and E. M. Stoudenmire, Codebase release 0.3 for ITensor, SciPost Phys. Codebases 4-r0.3 (2022).

[59] M. Lewenstein, A. Sanpera, and V. Ahufinger, *Ultracold Atoms in Optical Lattices: Simulating Quantum Many-Body Systems* (Oxford University Press, Oxford, 2012).

[60] R. Kenna and A. Irving, The Kosterlitz-Thouless universality class, Nucl. Phys. B **485**, 583 (1997).

[61] R. V. Pai and R. Pandit, Superfluid, Mott-insulator, and mass-density-wave phases in the one-dimensional extended Bose-Hubbard model, Phys. Rev. B **71**, 104508 (2005).

[62] B. V. Svistunov, Superfluid–Bose-glass transition in weakly disordered commensurate one-dimensional system, Phys. Rev. B **54**, 16131 (1996).

[63] J. Schönmeier-Kromer and L. Pollet, Ground-state phase diagram of the two-dimensional Bose-Hubbard model with anisotropic hopping, Phys. Rev. A **89**, 023605 (2014).

[64] S. Ejima, H. Fehske, and F. Gebhard, Dynamic properties of the one-dimensional Bose-Hubbard model, Europhys. Lett. **93**, 30002 (2011).

[65] A. Padhan, S. Mondal, S. Vishveshwara, and T. Mishra, Interacting bosons on a Su-Schrieffer-Heeger ladder: Topological phases and Thouless pumping, Phys. Rev. B **109**, 085120 (2024).

[66] R. V. Mishmash, M. S. Block, R. K. Kaul, D. N. Sheng, O. I. Motrunich, and M. P. A. Fisher, Bose metals and insulators on multileg ladders with ring exchange, Phys. Rev. B **84**, 245127 (2011).

[67] M. S. Block, R. V. Mishmash, R. K. Kaul, D. N. Sheng, O. I. Motrunich, and M. P. A. Fisher, Exotic gapless Mott insulators of bosons on multileg ladders, Phys. Rev. Lett. **106**, 046402 (2011).

[68] A. Potapova, I. Pilé, T.-C. Yi, R. Mondaini, and E. Burovski, Dimensional crossover on multileg attractive-U Hubbard ladders, Phys. Rev. A **107**, 053301 (2023).

[69] J. F. Wienand, S. Karch, A. Impertro, C. Schweizer, E. McCulloch, R. Vasseur, S. Gopalakrishnan, M. Aidelsburger, and I. Bloch, Emergence of fluctuating hydrodynamics in chaotic quantum systems, Nat. Phys. **20**, 1732 (2024).

[70] D. Wellnitz, G. A. Domínguez-Castro, T. Bilitewski, M. Aidelsburger, A. M. Rey, and L. Santos, Emergent interaction-induced topology in Bose-Hubbard ladders, Phys. Rev. Res. **7**, L012012 (2025).

[71] K. Wintersperger, C. Braun, F. N. Ünal, A. Eckardt, M. D. Liberto, N. Goldman, I. Bloch, and M. Aidelsburger, Realization of an anomalous Floquet topological system with ultracold atoms, Nat. Phys. **16**, 1058 (2020).

[72] R. Parida, A. Padhan, and T. Mishra, Interaction driven topological phase transitions of hardcore bosons on a two-leg ladder, Phys. Rev. B **110**, 165110 (2024).

[73] A. Lamacraft, Dispersion relation and spectral function of an impurity in a one-dimensional quantum liquid, Phys. Rev. B **79**, 241105(R) (2009).

[74] M. Schecter, A. Kamenev, D. M. Gangardt, and A. Lamacraft, Critical velocity of a mobile impurity in one-dimensional quantum liquids, Phys. Rev. Lett. **108**, 207001 (2012).

[75] N. A. Kamar, A. Kantian, and T. Giamarchi, Mobile impurity in a two-leg bosonic ladder, Phys. Rev. Res. **7**, 033136 (2025).

[76] S. Manna, C. W. Duncan, C. A. Weidner, J. F. Sherson, and A. E. B. Nielsen, Anyon braiding on a fractal lattice with a local Hamiltonian, Phys. Rev. A **105**, L021302 (2022).

[77] S. Manna, B. Jaworowski, and A. E. B. Nielsen, Many-body localization on finite generation fractal lattices, J. Stat. Mech. (2024) 053301.

[78] K. Dutkiewicz, M. Płodzień, A. Rojo-Francàs, B. Juliá-Díaz, M. Lewenstein, and T. Grass, Bose-Einstein condensation in exotic lattice geometries, Phys. Rev. A **113**, 013320 (2026).

[79] L. Carfora, C. W. Duncan, S. Kuhr, and P. Kirton, Data for "Mott-insulating phases of the Bose-Hubbard model on quasi-one-dimensional ladder lattices", 2026, doi:10.15129/dac2b14d-5cb2-4597-bb00-f8a155c91e5f.

[80] S. Sachdev, in *Quantum Magnetism*, edited by U. Schollwöck, J. Richter, D. J. J. Farnell, and R. F. Bishop, Lecture Notes in Physics Vol. 645 (Springer, Berlin, 2004), pp. 381–432.

[81] H. H. Roomany and H. W. Wyld, Finite-lattice approach to the O(2) and O(3) models in 1+1 dimensions and the (2+1)-dimensional Ising model, Phys. Rev. D **21**, 3341 (1980).

[82] A. Messiah, *Quantum Mechanics* (Courier, North Chelmsford, 2014).

[83] L. Wang, Y. Hao, and S. Chen, Preparation of stable excited states in an optical lattice via sudden quantum quench, Phys. Rev. A **81**, 063637 (2010).